

# Dipolar Spin Liquid Ending with Quantum Critical Point in a Gd-based Triangular Magnet

Junsen Xiang,<sup>1,\*</sup> Cheng Su,<sup>2,\*</sup> Ning Xi,<sup>3,\*</sup> Zhendong Fu,<sup>4</sup> Zhuo Chen,<sup>5</sup> Hai Jin,<sup>6</sup> Ziyu Chen,<sup>2</sup> Zhao-Jun Mo,<sup>7</sup> Yang Qi,<sup>8,9</sup> Jun Shen,<sup>5,10</sup> Long Zhang,<sup>11,12</sup> Wentao Jin,<sup>2,†</sup> Wei Li,<sup>3,12,13,‡</sup> Peijie Sun,<sup>1,§</sup> and Gang Su<sup>11,12,¶</sup>

<sup>1</sup>Beijing National Laboratory for Condensed Matter Physics,  
Institute of Physics, Chinese Academy of Sciences, Beijing 100190, China

<sup>2</sup>School of Physics, Beihang University, Beijing 100191, China

<sup>3</sup>CAS Key Laboratory of Theoretical Physics, Institute of Theoretical Physics, Chinese Academy of Sciences, Beijing 100190, China

<sup>4</sup>Neutron Platform, Songshan Lake Materials Laboratory, Dongguan 523808, China

<sup>5</sup>School of Mechanical Engineering, Beijing Institute of Technology, Beijing 100081, China

<sup>6</sup>Department of Astronomy, Tsinghua University, Beijing 100084, China

<sup>7</sup>Ganjiang Innovation Academy, Chinese Academy of Sciences, Ganzhou 341119, People's Republic of China.

<sup>8</sup>State Key Laboratory of Surface Physics, Fudan University, Shanghai 200433, China

<sup>9</sup>Center for Field Theory and Particle Physics, Department of Physics, Fudan University, Shanghai 200433, China

<sup>10</sup>Technical Institute of Physics and Chemistry, Chinese Academy of Sciences, Beijing 100190, China

<sup>11</sup>Kavli Institute for Theoretical Sciences, and School of Physical Sciences,

University of Chinese Academy of Sciences, Beijing 100049, China

<sup>12</sup>CAS Center for Excellence in Topological Quantum Computation,

University of Chinese Academy of Sciences, Beijing 100190, China

<sup>13</sup>Peng Huanwu Collaborative Center for Research and Education, Beihang University, Beijing 100191, China

(Dated: January 18, 2023)

By performing experiment and model studies on a triangular-lattice dipolar magnet  $\text{KBaGd}(\text{BO}_3)_2$  (KBGB), we find the highly frustrated magnet with a planar anisotropy hosts a strongly fluctuating dipolar spin liquid (DSL), which originates from the intriguing interplay between dipolar and Heisenberg interactions. The DSL constitutes an extended regime in the field-temperature phase diagram, which gets lowered in temperature as field increases and eventually ends with an unconventional quantum critical point (QCP) at  $B_c \simeq 0.75$  T. Based on the dipolar Heisenberg model analysis, the DSL is identified as a Berezinskii-Kosterlitz-Thouless (BKT) phase with emergent  $U(1)$  symmetry, and the end QCP belongs to the 3D XY universality class. Due to the tremendous entropy accumulation that can be related to the strong BKT and quantum fluctuations, unprecedented magnetic cooling effects are observed in the DSL and particularly near the QCP, making KBGB a superior dipolar coolant to commercial Gd-based refrigerants. We establish the phase diagram for triangular-lattice dipolar quantum magnets where emergent symmetry plays an essential role, and provide a basis and opens an avenue for their applications in sub-Kelvin refrigeration.

*Introduction.*— Triangular-lattice quantum antiferromagnets have raised great research interest recently due to the unusual quantum spin states and transitions therein [1, 2]. One prominent example is the quantum spin liquid (QSL) [3–5] and its possible materialization in organic compounds [6–8] and rare-earth triangular magnets [9–16]. The intriguing spin frustration effects and two dimensionality of such systems imply Berezinskii-Kosterlitz-Thouless (BKT) physics may appear at low temperatures. Indeed, the Co-based quantum antiferromagnet  $\text{Na}_2\text{BaCo}(\text{PO}_4)_2$  hosts persistent spin fluctuations [17–20] till very low temperature, and is proposed to realize spin supersolidity with prominent BKT phase fluctuations [21]. Besides, emergent symmetry has also been disclosed on the triangular lattice as a consequence of strong frustration, with a primary example of rare-earth magnet  $\text{TmMgGaO}_4$  [22–27].

Recently, it has been theoretically proposed that the dipolar interactions can give rise to QSL in triangular-lattice quantum spin systems [29]. Lately such dipolar system has been realized in Yb-based triangular compounds [30–34]. However, the dipolar interactions are rather weak and it is very challenging for conventional thermodynamic and spectroscopic measurements to probe the exotic spin states due to dipolar interactions. On the contrary, the rare-earth dipolar magnets

with even larger moments, *e.g.*, Gd-based compounds with  $\mu_{\text{eff}} \approx 8\mu_B$  and high spin  $S = 7/2$ , are much less explored both in experiments and theories. It is expected that the dipolar frustration effects are a priori more evident in these systems. Moreover, high-spin frustrated systems, especially those with spin-liquid like behaviors [35], can possess large entropy density and cooling capacity, holding thus strong promise as excellent coolants for sub-Kelvin space applications [36, 37] and quantum computing [38].

In this work, we perform low-temperature thermodynamic and magnetocaloric measurements on single-crystal samples of gadolinium borate  $\text{KBaGd}(\text{BO}_3)_2$  (KBGB). The thermodynamic measurements suggest a dipolar spin liquid state with no conventional ordering but strong spin fluctuations as reflected in the algebraic specific heat and imaginary dynamical susceptibility ( $\chi''_{\text{ac}}$ ). We establish a dipolar Heisenberg model with both dipole-dipole and Heisenberg interactions for KBGB. Monte Carlo (MC) simulations well explain the experimental results and unveil exotic spin states and transitions in the phase diagram. In particular, the model simulations suggest a two-step melting of the 6-clock antiferromagnetic (AF) order [c.f., Fig. 1(c)] via two BKT transitions, between which a floating BKT phase appears with an emergent  $U(1)$  symmetry, well accounting for the experimental observations.

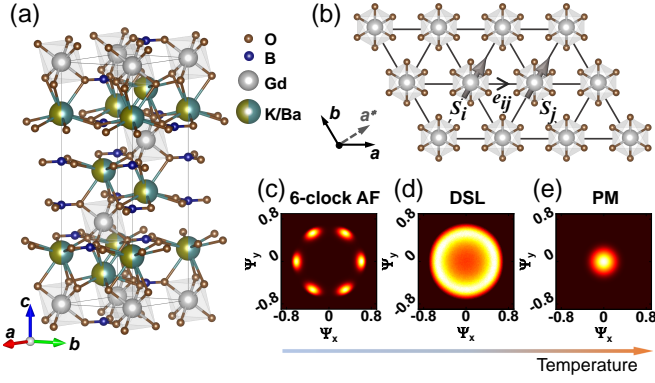


FIG. 1. (a) shows the crystal structure of KBaGd(BO<sub>3</sub>)<sub>2</sub>, and (b) the triangular-lattice layers of GdO<sub>6</sub> octahedra separated by the Ba/K layers with site mixing. The grey arrows refer to the spins on site  $i$  and  $j$ , and the unit vector  $e_{ij}$  is also indicated. Dipole-dipole interactions are bond-dependent and follow the  $\bar{3}m$  site symmetry. (c)-(e) are histograms of the order parameter  $\Psi_{xy} \equiv \Psi_x + i\Psi_y$  for the 6-clock antiferromagnetic (AF) phase, emergent U(1) dipolar spin liquid (DSL), and paramagnetic (PM) phase [28].

Consequently, giant magnetocaloric effect (MCE) is observed in the quasi-adiabatic demagnetization measurements. In particular, we find a clear dip in temperature at  $B_c \simeq 0.75$  T, i.e., near the quantum critical point (QCP) also with emergent U(1) symmetry. The obtained lowest temperature of 70 mK clearly surpasses that of commercial refrigerant Gd<sub>3</sub>Ga<sub>5</sub>O<sub>12</sub> (GGG) under similar conditions, opening an avenue for exploring not only exotic spin states and transitions but also superior quantum coolants.

*Crystal structure and effective model for KBaGd(BO<sub>3</sub>)<sub>2</sub>.*— Centimeter-sized single crystals of KBGB were synthesized using the flux method as described in detail in Supplementary Materials (SM) [28]. X-ray diffraction measurements indicate high quality of the single crystals, and confirm the trigonal structure [40, 41] with space group  $R\bar{3}m$  [c.f., Fig. 1(a)]. Magnetic Gd<sup>3+</sup> ions with  $4f^7$  electron configuration ( $L = 0$ ,  $S = 7/2$ ) form perfect triangular lattice [Fig. 1(b)], with a relatively high ionic density of  $6.4 \text{ nm}^{-3}$ .

The direct dipolar interaction between magnetic ions Gd<sup>3+</sup> has a characteristic energy  $E_{\text{dp}} \sim 2\mu_0\mu_{\text{sat}}^2/4\pi a^3 \approx 0.05 \text{ meV}$  (with  $\mu_{\text{sat}} \approx 8 \mu_B$ ), which determines the low-temperature spin states in KBGB. To simulate the dipolar magnet, we consider the Hamiltonian  $H = J_H \sum_{\langle i,j \rangle_{\text{NN}}} \mathbf{S}_i \cdot \mathbf{S}_j + J_D \sum_{i,j} [\mathbf{S}_i \cdot \mathbf{S}_j - 3(\mathbf{S}_i \cdot \mathbf{e}_{ij})(\mathbf{S}_j \cdot \mathbf{e}_{ij})]/r_{ij}^3$ , where  $\mathbf{e}_{ij}(r_{ij})$  refers to the unit vector(distance) between site  $i$  and  $j$  in the unit of lattice constant  $a$ .  $J_H$  and  $J_D$  refer to the nearest neighbor (NN) Heisenberg and dipole-dipole interactions, respectively. As the dipolar interactions show rapid (cubic) power-law decay with longer range interactions washed out, below we keep only NN terms

$$H_{\text{DH}} = \sum_{\langle i,j \rangle_{\text{NN}}} J \mathbf{S}_i \cdot \mathbf{S}_j - D (\mathbf{S}_i \cdot \mathbf{e}_{ij})(\mathbf{S}_j \cdot \mathbf{e}_{ij}), \quad (1)$$

where  $J = J_H + J_D$  is the NN isotropic coupling and

$D = 3J_D$  refers to the dipolar anisotropic term. We perform MC simulations of the NN dipolar Heisenberg (DH) model on up to  $60 \times 60$  triangular lattice [28], and find the results fit very well the experimental results. The determined coupling parameters from the fittings are  $J \simeq 47 \text{ mK}$  and  $D \simeq 80 \text{ mK}$ , which correspond to  $J_D \simeq 27 \text{ mK}$  and  $J_H \simeq 20 \text{ mK}$ , leading to a dipolar energy of about 660 mK. Such estimate based on MC fittings is consistent with the direct interaction of  $E_{\text{dp}} \approx 0.05 \text{ meV}$  evaluated above.

*Magnetic specific heat, susceptibility, and dipolar spin liquid.*— In Fig. 2(a) we show the zero-field specific heat  $C_m$  measured down to 65 mK for KBGB. There exists a round peak at  $T^* \simeq 209 \text{ mK}$ , below which the system exhibits  $C_m \sim T^2$  with algebraic scaling, resembling that of two-dimensional (2D) Heisenberg or XY quantum spin model with U(1) symmetry [42, 43]. The thermodynamic measurements suggest a gapless liquid-like and strongly fluctuating spin state as if the dipolar planar anisotropy were absent. This is also reflected in the huge low-temperature specific heat in KBGB, which far exceeds that of the renowned Gd-based refrigerant GGG [37, 39, 44].

In Fig. 2(b), we apply out-of-plane fields ( $B//c$ ) to the compound, and find the round  $C_m$  peaks move towards lower temperature with heights slightly reduced. This suggests that the spin liquid states constitute an extended phase that we dub as *dipolar spin liquid* (DSL). As field further increases and exceeds about 0.75 T, the DSL behavior disappears [c.f., the contour plot of  $C_m/T$  in Fig. 3(b)], and the  $C_m$  peaks move instead to the high-temperature side with low-energy fluctuations quickly suppressed.

Fig. 2(c) shows the isothermal magnetization measured at  $T = 0.4 \text{ K}$ , where a clear magnetic anisotropy between the out-of-plane ( $//c$  axis) and in-plane ( $//a$ ) directions is observed. This anisotropy can be clearly recognized in the different saturation magnetization moments, and the transition fields are also different along two directions, i.e., about 1 T (0.5 T) along  $c(a)$  axis. Likewise, the low-temperature dc susceptibility ( $\chi_{\text{dc}}$ ) exhibits a clear easy-plane anisotropy, see Fig. 2(d). Although the determined Landé factor  $g_c \simeq 2.49$  is slightly larger than  $g_a \simeq 2.36$ , the intrinsic dipolar anisotropy leads to larger in-plane  $\chi_{\text{dc}}$  (along  $a$  and  $a^*$  axes) than that along the  $c$  axis. The negative Curie-Weiss temperatures fitted from the dc susceptibility reflect the AF nature, and the slightly different  $\theta_a \simeq -300 \text{ mK}$  and  $\theta_{a^*} \simeq -330 \text{ mK}$  reveal the planar anisotropy. This small but sensible planar anisotropy between  $a$  and  $a^*$  axes can be ascribed to the bond-dependent dipolar interaction [c.f., Eq. (1)].

The proposed DSL is further corroborated by the ac magnetic susceptibilities shown in Figs. 2(e,f). The real part  $\chi'_{\text{ac}}$  exhibits a frequency-independent maximum and remains large even below the characteristic temperature  $T^*$ . The spin-glass scenario is therefore firmly excluded despite the K/Ba site mixing in the compound. Interestingly, the imaginary ac susceptibility  $\chi''_{\text{ac}}(T)$ , although being featureless for low frequencies  $\omega \lesssim 4 \text{ kHz}$ , show a clear temperature-dependent behavior for higher frequencies in Fig. 2(f). Considering that

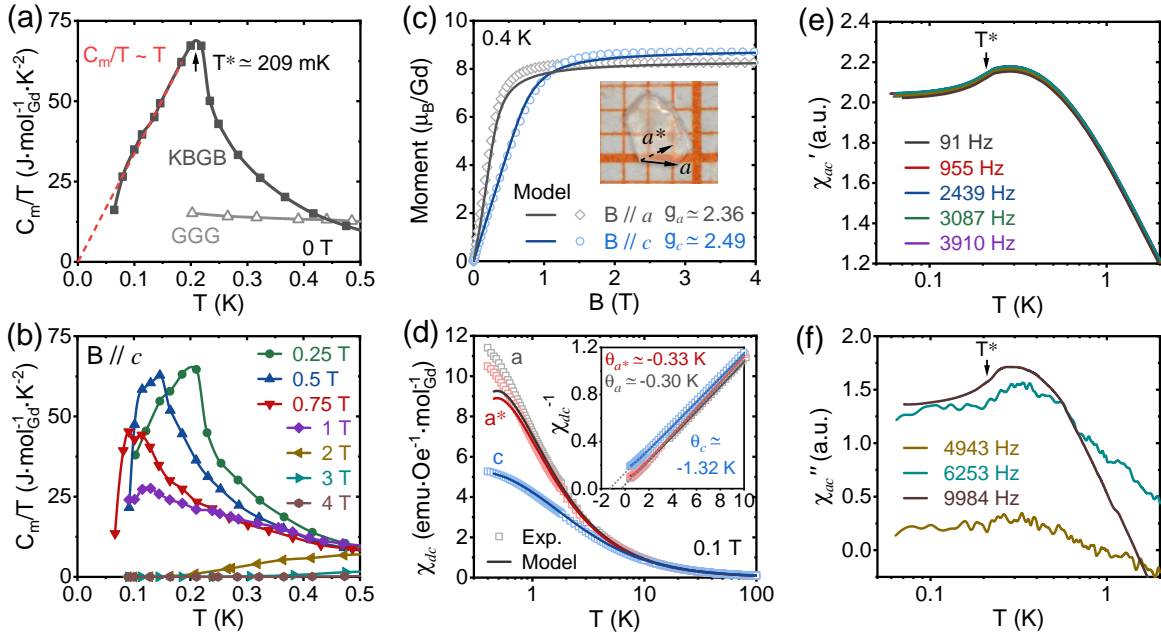


FIG. 2. Specific heat of KBGB under (a) zero and (b) finite fields along out-of-plane direction. An algebraic  $C_m \sim T^2$  scaling is observed below the peak temperature  $T^*$  in (a), where the  $C_m/T$  values far outweigh that of GGG [39]. (c) shows the magnetization curves of the single-crystal KBGB sample for  $B//a$  and  $//c$ , and the results show excellent agreement with the DH model calculations (solid lines). The saturation moments are  $\mu_a^{\text{sat}} \simeq 8.26\mu_B$  and  $\mu_c^{\text{sat}} \simeq 8.72\mu_B$ , from which we determine the Landé factors  $g_a \simeq 2.36$  and  $g_c \simeq 2.49$ , respectively. The as-grown KBGB single crystal is shown in the inset, with directions  $a$  and  $a^*$  also indicated. (d) shows the molar dc magnetic susceptibilities ( $\chi_{\text{dc}}$ ) measured along the  $a$ ,  $a^*$ , and  $c$  axes, respectively, where the solid lines representing the DH model calculations show excellent agreements. The inset shows the Curie-Weiss fittings in the paramagnetic regime  $0.4 \text{ K} \leq T \leq 10 \text{ K}$ , with the fitted Curie-Weiss temperatures  $\theta_{a^*} \simeq -0.33 \text{ K}$ ,  $\theta_a \simeq -0.30 \text{ K}$ , and  $\theta_c \simeq -1.32 \text{ K}$ . (e, f) present respectively the real and imaginary ac susceptibilities measured with different frequencies.

$\chi''(\omega)$  can be directly related to the dynamical correlation  $S(\omega)$  through the fluctuation-dissipation theorem,  $\chi''(\omega) \propto \frac{\omega}{T} S(\omega)$  ( $\omega \ll T$ ), this clearly suggests the persistence of low-energy spin fluctuations even below  $T^*$  and supports the spin-liquid scenario.

**Magnetocaloric effect and quantum critical point.**— In Fig. 3(a), we show the quasi-adiabatic demagnetization measurements (see details in SM [28]), where the lowest temperature  $T_m$  is achieved around the dip  $B_c \simeq 0.75 \text{ T}$  in the isentropic line and remains at very low temperature for  $B < B_c$  in the small field side. In particular, it is found that KBGB clearly outperforms GGG in the obtained lowest temperature, *i.e.*,  $T_m \simeq 70 \text{ mK}$  (KBGB) vs.  $322 \text{ mK}$  (GGG), for the same initial condition of  $T_i = 2 \text{ K}$  and  $B_i = 6 \text{ T}$ . In Fig. 3(b) we provide more of the isentropic lines from different initial conditions, and observe the highly asymmetric isentropes, which “levels off” in the bright DSL regime with strong fluctuations reflected in large  $C_m/T$ .

Remarkably, strong cooling effects are also observed for very low, sub-Kelvin initial temperature. In Fig. 3(b), we obtain a lowest  $T_m \simeq 33 \text{ mK}$  from initial  $T_i \simeq 95 \text{ mK}$ . Such unprecedented MCE response strongly corroborates the existence of QCP at  $B_c \simeq 0.75 \text{ T}$ , as is further substantiated by an evident peak-dip structure with sign change in the magnetic Grüneisen ratio  $\Gamma_B = \frac{1}{T} \left( \frac{\partial T}{\partial B} \right)_S$  [45–48], shown in Fig. 3 in-

set, which has been widely used in characterizing QCP for heavy fermions [49–53] and low-dimensional quantum spin systems [54–57]. The peak height of  $\Gamma_B$  exceeds 4 times that of GGG, indicating a giant QCP cooling effect in KBGB.

**Emergent symmetry in KBGB.**— According to the above measurements, we obtain the phase diagram of KBGB in Fig. 3(b). The two schematic dashed lines, enclosing the DSL with large  $C_m/T$  values, meet at a QCP where the lowest cooling temperature is reached. Besides QCP, within the DSL regime we find persistent spin fluctuations and cooling effects whose origin is clarified through a model analysis below.

In Figs. 2(c,d), we find the anisotropic susceptibility and magnetization measured along  $a$  and  $c$  axes can be well captured by the DH model. The slight deviation between model calculations and experimental in-plane susceptibilities at low temperature  $\lesssim 0.5 \text{ K}$  may be attributed to strong quantum fluctuations of planar order parameters. Besides, the model calculations find a specific heat peak at about  $270 \text{ mK}$ , which also gets suppressed as field increases, well resembling the experimental results in Figs. 2(a,b). As various phases with prominent features are well captured by MC simulations [28], we thus confirm that the DH model can very well describe the dipolar magnet KBGB.

To characterize the spin states in the phase diagram, we introduce the order parameter  $\Psi_{xy} \equiv m e^{i\theta} = \sum_j e^{iQr_j} (m_j^x +$

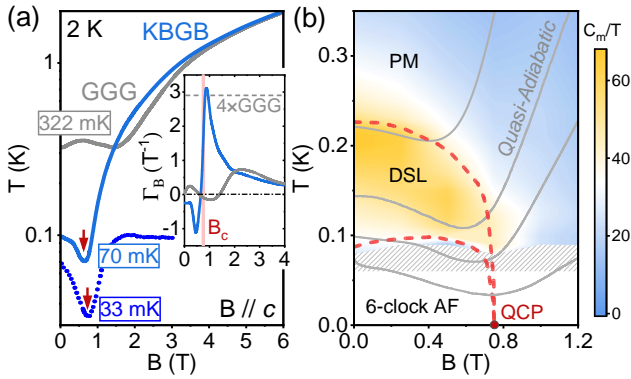


FIG. 3. (a) shows the quasi-adiabatic isentropes measured in KBGB under out-of-plane fields. The KBGB curve exhibits a clear dip at the lowest temperature  $T_m \simeq 70$  mK, much lower than that of GGG ( $T_m \simeq 322$  mK). Starting from  $T_i \simeq 95$  mK, KBGB can reach a remarkably low temperature  $T_m \simeq 33$  mK in the dip (blue dotted line). The inset shows the magnetic Grüneisen ratio  $\Gamma_B$  deduced from the curves in the main panel. (b) shows the phase diagram of KBGB with the  $C_m/T$  contour plot in the background. The bright regime with large spin fluctuations represent the DSL, with schematic dashed line boundaries, ending with a QCP at  $B_c \simeq 0.75$  T.

$im_j^y$ ), where  $j$  runs over the lattice sites and  $Q = \pm \frac{1}{2}a^*, \pm \frac{1}{2}b^*, \pm \frac{1}{2}(a^* - b^*)$  [28]. Histogram of the complex order parameter  $\Psi_{xy}$  at various temperature are shown in Figs. 1(c-e). At low temperature, the dipolar system exhibits a 6-clock AF order corresponding to  $\theta = 0, \pm\pi/3, \pm 2\pi/3$ , and  $\pi$  [28]. As temperature ramps up, the six points in the histogram prolong and merge into a circle with emergent U(1) symmetry, where the angle  $\theta$  can choose arbitrary angle. As temperature further enhances, the amplitude  $m$  eventually vanishes and the system enters the conventional PM phase.

Recall that the 6-state clock model with  $\cos(6\theta)$  anisotropic term undergoes two successive BKT transitions [58], between which the anisotropic term becomes irrelevant perturbation, the intermediate DSL thus constitutes a BKT phase with emergent U(1) symmetry [59–62]. For the zero-temperature QCP, as the clock term is dangerously irrelevant there [59], transition occurs directly between the 6-clock AF and PM phases and belongs to the 3D XY universality class. The corresponding critical exponents  $z = 1$  and  $\nu \simeq 0.66$  [63] can lead to a strongly diverging  $\Gamma_B \sim T^{-1/z\nu}$  [45], which may account for the very sharp peak observed in Fig. 3(a) inset. Therefore, emergent symmetry constitutes a key for understanding the spin liquid and quantum criticality in KBGB.

*Superior cooling performance.*— Starting from  $T_i = 2$  K, KBGB single crystals are observed to reach  $T_m \simeq 70$  mK [Fig. 3(a)], far surpassing other Gd-based refrigerants, *e.g.*, GGG (322 mK) and GdLiF<sub>4</sub> (480 mK) [65]. Besides, powder samples can also achieve much lower  $T_m$  than that of GGG [28]. Long hold time  $t_h$  is also witnessed in KBGB. In the environment temperature of 2 K, it remains below 140 mK for  $t_h \simeq 2$  h after the field is exhausted, which can be ascribed

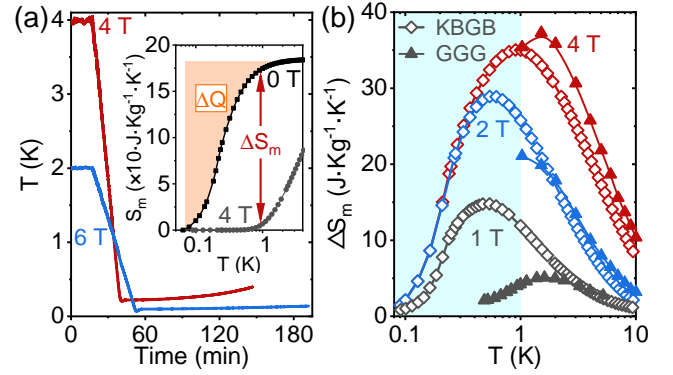


FIG. 4. (a) The quasi-adiabatic demagnetization cooling curves of KBGB single-crystal sample (0.5 g), starting from two different initial conditions ( $T_i = 4$  K,  $B_i = 4$  T) and ( $T_i = 2$  K,  $B_i = 6$  T), and reaching lowest temperature  $T_m \simeq 205$  mK and 70 mK, respectively. Parasitic heat loads are estimated to be  $0.2 \mu\text{W}$  for  $T_i = 4$  K environment and  $0.05 \mu\text{W}$  for  $T_i = 2$  K. The inset shows magnetic entropy under zero and 4 T fields, with the shaded area representing the absorbed heat  $\Delta Q = 47.44 \text{ J}\cdot\text{Kg}^{-1}$  in the hold process. (b) plots the entropy change results  $\Delta S_m$  vs.  $T$ , for fields decreasing from various peak values to zero, and compared to those of GGG [39, 64].

to the large heat absorption  $\Delta Q$  shown in inset of Fig. 4(a). The isothermal entropy change  $\Delta S_m$  characterizes the cooling capacity of refrigerants. In Fig. 4(b), we compare  $\Delta S_m$  of KBGB with that of GGG, and find that KBGB has significantly larger  $\Delta S_m$  below 1 K [shaded regime in Fig. 4(b)], *i.e.*, the temperature window of central interest for sub-Kelvin application. Overall, the low cooling temperature  $T_m$ , long hold time  $t_h$ , and giant entropy change  $\Delta S_m$  suggest that KBGB is a superior quantum magnet coolant for cryogenics.

*Discussions and outlook.*— The pursue for high entropy density and low ordering temperature constitutes two opposing factors hard to fulfill simultaneously for sub-Kelvin refrigerants. Here we find the spin frustration and quantum criticality in the dipolar system come to the rescue. We show that the compound KBaGd(BO<sub>3</sub>)<sub>2</sub> with high density Gd<sup>3+</sup> crystallizing on a triangular lattice is demonstrated to host a disordered and strongly fluctuating spin liquid till very low temperature, offering enormous cooling capacity. This can be ascribed to the prominent BKT fluctuations and quantum criticality in this  $S = 7/2$  dipolar magnet. Despite a planar anisotropy, U(1) symmetry nevertheless emerges in the compound as revealed by the DH model analysis. Although in the present study only NN terms are considered, inclusion of further neighboring couplings is believed not to change the conclusion here, as it maintains the universality class of BKT transitions in the planar dipolar models [62, 66].

The scenario of DSL ending up with emergent U(1) QCP may also be applicable to other dipolar quantum magnets. Recent progress in experimental studies reveal a series of rare-earth triangular quantum dipolar antiferromagnets, *e.g.*, Ba<sub>3</sub>REB<sub>3</sub>O<sub>9</sub>/Ba<sub>3</sub>REB<sub>9</sub>O<sub>18</sub> (with RE a rare-earth ion) [32, 33] and ABaRE(BO<sub>3</sub>)<sub>2</sub> (with A an alkali ion) [67, 68]. For exam-

ple, it has been observed that in  $\text{Ba}_3\text{YbB}_3\text{O}_9$  that 80% entropy remain below 56 mK [31], despite a dipolar interaction of about 160 mK, suggesting that the DSL and unconventional QCP may also be relevant in the Yb-based dipolar compounds. This work, therefore, opens a venue for hunting exotic spin states as well as superior quantum coolants in triangular dipolar magnets.

*Note added.*— Upon finishing the present work, we are aware of a recent work [69] also that also conducts the MCE study of KBGB with however polycrystalline samples, where they find strong cooling effect down to 121 mK.

*Acknowledgements.*— W.L. is indebted to Yuan Wan and Tao Shi for helpful discussions. W.J. and C.S. acknowledge the support from the beamline 1W1A of the Beijing Synchrotron Radiation Facility. This work was supported by the National Natural Science Foundation of China (Grant Nos. 1222412, 11834014, 11974036, 12047503, 12074023, 12074024, 12174387, and 12141002), National Key R & D Program of China (Grant No. 2018YFA0305800), Strategic Priority Research Program of CAS (Grant No. XDB28000000), and CAS Project for Young Scientists in Basic Research (Grant No. YSBR-057). We thank the HPC-ITP for the technical support and generous allocation of CPU time. This work was supported by the Synergetic Extreme Condition User Facility (SECUF).

\* These authors contributed equally to this work.

† wtjin@buaa.edu.cn

‡ w.li@itp.ac.cn

§ pjsun@iphy.ac.cn

¶ gsu@ucas.ac.cn

- [1] M. F. Collins and O. A. Petrenko, Review/synthèse: Triangular antiferromagnets, *Can. J. Phys.* **75**, 605 (1997).
- [2] O. A. Starykh, Unusual ordered phases of highly frustrated magnets: a review, *Rep. Prog. Phys.* **78**, 052502 (2015).
- [3] P. W. Anderson, Resonating valence bonds: A new kind of insulator?, *Mater. Res. Bull.* **8**, 153 (1973).
- [4] Y. Zhou, K. Kanoda, and T.-K. Ng, Quantum spin liquid states, *Rev. Mod. Phys.* **89**, 025003 (2017).
- [5] L. Balents, Spin liquids in frustrated magnets, *Nature* **464**, 199 (2010).
- [6] Y. Shimizu, K. Miyagawa, K. Kanoda, M. Maesato, and G. Saito, Spin liquid state in an organic Mott insulator with a triangular lattice, *Phys. Rev. Lett.* **91**, 107001 (2003).
- [7] M. Yamashita, N. Nakata, Y. Senshu, M. Nagata, H. M. Yamamoto, R. Kato, T. Shibauchi, and Y. Matsuda, Highly mobile gapless excitations in a two-dimensional candidate quantum spin liquid, *Science* **328**, 1246 (2010).
- [8] K. Kanoda and R. Kato, Mott physics in organic conductors with triangular lattices, *Annu. Rev. Condens. Matter Phys.* **2**, 167 (2011).
- [9] Y. Li, H. Liao, Z. Zhang, S. Li, F. Jin, L. Ling, L. Zhang, Y. Zou, L. Pi, Z. Yang, J. Wang, Z. Wu, and Q. Zhang, Gapless quantum spin liquid ground state in the two-dimensional spin-1/2 triangular antiferromagnet  $\text{YbMgGaO}_4$ , *Sci. Rep.* **5**, 16419 (2015).
- [10] Y. Li, G. Chen, W. Tong, L. Pi, J. Liu, Z. Yang, X. Wang, and Q. Zhang, Rare-earth triangular lattice spin liquid: A single-crystal study of  $\text{YbMgGaO}_4$ , *Phys. Rev. Lett.* **115**, 167203 (2015).
- [11] Y. Shen, Y.-D. Li, H. Wo, Y. Li, S. Shen, B. Pan, Q. Wang, H. C. Walker, P. Steffens, M. Boehm, Y. Hao, D. L. Quintero-Castro, L. W. Harriger, M. D. Frontzek, L. Hao, S. Meng, Q. Zhang, G. Chen, and J. Zhao, Evidence for a spinon fermi surface in a triangular-lattice quantum-spin-liquid candidate, *Nature* **540**, 559 (2016).
- [12] J. A. M. Paddison, M. Daum, Z. Dun, G. Ehlers, Y. Liu, M. B. Stone, H. Zhou, and M. Mourigal, Continuous excitations of the triangular-lattice quantum spin liquid  $\text{YbMgGaO}_4$ , *Nat. Phys.* **13**, 117 (2017).
- [13] Y. Shen, Y.-D. Li, H. C. Walker, P. Steffens, M. Boehm, X. Zhang, S. Shen, H. Wo, G. Chen, and J. Zhao, Fractionalized excitations in the partially magnetized spin liquid candidate  $\text{YbMgGaO}_4$ , *Nat. Commun.* **9**, 4138 (2018).
- [14] W. Liu, Z. Zhang, J. Ji, Y. Liu, J. Li, X. Wang, H. Lei, G. Chen, and Q. Zhang, Rare-earth chalcogenides: A large family of triangular lattice spin liquid candidates, *Chin. Phys. Lett.* **35**, 117501 (2018).
- [15] M. M. Bordelon, E. Kenney, C. Liu, T. Hogan, L. Posthuma, M. Kavand, Y. Lyu, M. Sherwin, N. P. Butch, C. Brown, M. J. Graf, L. Balents, and S. D. Wilson, Field-tunable quantum disordered ground state in the triangular-lattice antiferromagnet  $\text{NaYbO}_2$ , *Nat. Phys.* **15**, 1058 (2019).
- [16] P.-L. Dai, G. Zhang, Y. Xie, C. Duan, Y. Gao, Z. Zhu, E. Feng, Z. Tao, C.-L. Huang, H. Cao, A. Podlesnyak, G. E. Granroth, M. S. Everett, J. C. Neufeind, D. Voneshen, S. Wang, G. Tan, E. Morosan, X. Wang, H.-Q. Lin, L. Shu, G. Chen, Y. Guo, X. Lu, and P. Dai, Spinon fermi surface spin liquid in a triangular lattice antiferromagnet  $\text{NaYbSe}_2$ , *Phys. Rev. X* **11**, 021044 (2021).
- [17] R. Zhong, S. Guo, G. Xu, Z. Xu, and R. J. Cava, Strong quantum fluctuations in a quantum spin liquid candidate with a Co-based triangular lattice, *Proc. Natl. Acad. Sci. U.S.A.* **116**, 14505 (2019).
- [18] N. Li, Q. Huang, X. Y. Yue, W. J. Chu, Q. Chen, E. S. Choi, X. Zhao, H. D. Zhou, and X. F. Sun, Possible itinerant excitations and quantum spin state transitions in the effective spin-1/2 triangular-lattice antiferromagnet  $\text{Na}_2\text{BaCo}(\text{PO}_4)_2$ , *Nat. Commun.* **11**, 4216 (2020).
- [19] S. Lee, C. H. Lee, A. Berlie, A. D. Hillier, D. T. Adroja, R. Zhong, R. J. Cava, Z. H. Jang, and K.-Y. Choi, Temporal and field evolution of spin excitations in the disorder-free triangular antiferromagnet  $\text{Na}_2\text{BaCo}(\text{PO}_4)_2$ , *Phys. Rev. B* **103**, 024413 (2021).
- [20] C. Wellm, W. Roscher, J. Zeisner, A. Alfonsov, R. Zhong, R. J. Cava, A. Savoyant, R. Hayn, J. van den Brink, B. Büchner, O. Janson, and V. Kataev, Frustration enhanced by Kitaev exchange in a  $j_{\text{eff}} = \frac{1}{2}$  triangular antiferromagnet, *Phys. Rev. B* **104**, L100420 (2021).
- [21] Y. Gao, Y.-C. Fan, H. Li, F. Yang, X.-T. Zeng, X.-L. Sheng, R. Zhong, Y. Qi, Y. Wan, and W. Li, Spin supersolidity in nearly ideal easy-axis triangular quantum antiferromagnet  $\text{Na}_2\text{BaCo}(\text{PO}_4)_2$ , *npj Quantum Mater.* **7**, 89 (2022).
- [22] F. A. Cevallos, K. Stolze, T. Kong, and R. J. Cava, Anisotropic magnetic properties of the triangular plane lattice material  $\text{TmMgGaO}_4$ , *Mater. Res. Bull.* **105**, 154 (2018).
- [23] Y. Shen, C. Liu, Y. Qin, S. Shen, Y.-D. Li, R. Bewley, A. Schneidewind, G. Chen, and J. Zhao, Intertwined dipolar and multipolar order in the triangular-lattice magnet  $\text{TmMgGaO}_4$ , *Nat. Commun.* **10**, 4530 (2019).
- [24] Y. Li, S. Bachus, H. Deng, W. Schmidt, H. Thoma, V. Hutnanu, Y. Tokiwa, A. A. Tsirlin, and P. Gegenwart, Partial up-up-

- down order with the continuously distributed order parameter in the triangular antiferromagnet  $\text{TmMgGaO}_4$ , *Phys. Rev. X* **10**, 011007 (2020).
- [25] H. Li, Y. D. Liao, B.-B. Chen, X.-T. Zeng, X.-L. Sheng, Y. Qi, Z. Y. Meng, and W. Li, Kosterlitz-Thouless melting of magnetic order in the triangular quantum Ising material  $\text{TmMgGaO}_4$ , *Nat. Commun.* **11**, 1111 (2020).
- [26] Z. Hu, Z. Ma, Y.-D. Liao, H. Li, C. Ma, Y. Cui, Y. Shangguan, Z. Huang, Y. Qi, W. Li, Z. Y. Meng, J. Wen, and W. Yu, Evidence of the Berezinskii-Kosterlitz-Thouless phase in a frustrated magnet, *Nat. Commun.* **11**, 5631 (2020).
- [27] Z. Dun, M. Daum, R. Baral, H. E. Fischer, H. Cao, Y. Liu, M. B. Stone, J. A. Rodriguez-Rivera, E. S. Choi, Q. Huang, H. Zhou, M. Mourigal, and B. A. Frandsen, Neutron scattering investigation of proposed Kosterlitz-Thouless transitions in the triangular-lattice ising antiferromagnet  $\text{TmMgGaO}_4$ , *Phys. Rev. B* **103**, 064424 (2021).
- [28] Supplementary Sec. 1 describes the KBGB sample preparation and their XRD characterization. The thermodynamic and magnetocaloric measurements are elaborated in Sec. 2, and Sec. 3 is devoted to the HD model calculations.
- [29] N. Y. Yao, M. P. Zaletel, D. M. Stamper-Kurn, and A. Vishwanath, A quantum dipolar spin liquid, *Nat. Phys.* **14**, 405 (2018).
- [30] K. Y. Zeng, L. Ma, Y. X. Gao, Z. M. Tian, L. S. Ling, and L. Pi, NMR study of the spin excitations in the frustrated antiferromagnet  $\text{Yb}(\text{BaBO}_3)_3$  with a triangular lattice, *Phys. Rev. B* **102**, 045149 (2020).
- [31] R. Bag, M. Ennis, C. Liu, S. E. Dissanayake, Z. Shi, J. Liu, L. Balents, and S. Haravifard, Realization of quantum dipoles in triangular lattice crystal  $\text{Ba}_3\text{Yb}(\text{BO}_3)_3$ , *Phys. Rev. B* **104**, L220403 (2021).
- [32] H. Cho, S. J. Blundell, T. Shiroka, K. MacFarquharson, D. Prabhakaran, and R. Coldea, Studies on Novel Yb-based Candidate Triangular Quantum Antiferromagnets:  $\text{Ba}_3\text{YbB}_3\text{O}_9$  and  $\text{Ba}_3\text{YbB}_9\text{O}_{18}$ , [arXiv:2104.01005](https://arxiv.org/abs/2104.01005) (2021).
- [33] J. Khatua, M. Pregelj, A. Elghandour, Z. Jagličić, R. Klingeler, A. Zorko, and P. Khuntia, Magnetic properties of triangular lattice antiferromagnets  $\text{Ba}_3\text{RB}_9\text{O}_{18}$  ( $R = \text{Yb}, \text{Er}$ ), *Phys. Rev. B* **106**, 104408 (2022).
- [34] C. Y. Jiang, Y. X. Yang, Y. X. Gao, Z. T. Wan, Z. H. Zhu, T. Shiroka, C. S. Chen, Q. Wu, X. Li, J. C. Jiao, K. W. Chen, Y. Bao, Z. M. Tian, and L. Shu, Spin excitations in the quantum dipolar magnet  $\text{Yb}(\text{BaBO}_3)_3$ , *Phys. Rev. B* **106**, 014409 (2022).
- [35] X.-Y. Liu, Y. Gao, H. Li, W. Jin, J. Xiang, H. Jin, Z. Chen, W. Li, and G. Su, Quantum spin liquid candidate as superior refrigerator in cascade demagnetization cooling, *Commun. Phys.* **108**, 233 (2022).
- [36] C. Hagemann and P. L. Richards, Adiabatic demagnetization refrigerators for small laboratory experiments and space astronomy, *Cryogenics* **35**, 303 (1995).
- [37] P. J. Shirron, Applications of the magnetocaloric effect in single-stage, multi-stage and continuous adiabatic demagnetization refrigerators, *Cryogenics* **62**, 130 (2014).
- [38] A. E. Jahromi, P. J. Shirron, and M. J. DiPirro, *Sub-Kelvin Cooling Systems for Quantum Computers*, Tech. Rep. (NASA Goddard Space Flight Center Greenbelt, MD, United States, 2019).
- [39] P. Schiffer, A. P. Ramirez, D. A. Huse, and A. J. Valentino, Investigation of the field induced antiferromagnetic phase transition in the frustrated magnet: Gadolinium gallium garnet, *Phys. Rev. Lett.* **73**, 2500 (1994).
- [40] M. B. Sanders, F. A. Cevallos, and R. J. Cava, Magnetism in the  $\text{KBaRE}(\text{BO}_3)_2$  ( $\text{RE} = \text{Sm}, \text{Eu}, \text{Gd}, \text{Tb}, \text{Dy}, \text{Ho}, \text{Er}, \text{Tm}, \text{Yb}, \text{Lu}$ ) series: materials with a triangular rare earth lattice, *Mater. Res. Express* **4**, 036102 (2017).
- [41] S. Guo, T. Kong, F. A. Cevallos, K. Stolze, and R. Cava, Crystal growth, crystal structure and anisotropic magnetic properties of  $\text{KBaR}(\text{BO}_3)_2$  ( $R = \text{Y}, \text{Gd}, \text{Tb}, \text{Dy}, \text{Ho}, \text{Tm}, \text{Yb}$  and  $\text{Lu}$ ) triangular lattice materials, *J. Magn. Magn. Mater.* **472**, 104 (2019).
- [42] P. Hasenfratz and F. Niedermayer, Finite size and temperature effects in the AF heisenberg model, *Z. Phys., B Condens. matter* **92**, 91 (1993).
- [43] A. W. Sandvik and C. J. Hamer, Ground-state parameters, finite-size scaling, and low-temperature properties of the two-dimensional  $S = \frac{1}{2}$  XY model, *Phys. Rev. B* **60**, 6588 (1999).
- [44] J. A. Paddison, H. Jacobsen, O. A. Petrenko, M. T. Fernández-Díaz, P. P. Deen, and A. L. Goodwin, Hidden order in spin-liquid  $\text{Gd}_3\text{Ga}_5\text{O}_{12}$ , *Science* **350**, 179 (2015).
- [45] L. J. Zhu, M. Garst, A. Rosch, and Q. M. Si, Universally Diverging Grüneisen Parameter and the Magnetocaloric Effect Close to Quantum Critical Points, *Phys. Rev. Lett.* **91**, 066404 (2003).
- [46] J.-S. Xiang, C. Chen, W. Li, X.-L. Sheng, N. Su, Z.-H. Cheng, Q. Chen, and Z.-Y. Chen, Criticality-enhanced magnetocaloric effect in quantum spin chain material copper nitrate, *Sci. Rep.* **7**, 44643 (2017).
- [47] M. Garst and A. Rosch, Sign change of the Grüneisen parameter and magnetocaloric effect near quantum critical points, *Phys. Rev. B* **72**, 205129 (2005).
- [48] T. Liu, X.-Y. Liu, Y. Gao, H. Jin, J. He, X.-L. Sheng, W. Jin, Z. Chen, and W. Li, Significant inverse magnetocaloric effect induced by quantum criticality, *Phys. Rev. Research* **3**, 033094 (2021).
- [49] Y. Tokiwa, T. Radu, C. Geibel, F. Steglich, and P. Gegenwart, Divergence of the Magnetic Grüneisen Ratio at the Field-Induced Quantum Critical Point in  $\text{YbRh}_2\text{Si}_2$ , *Phys. Rev. Lett.* **102**, 066401 (2009).
- [50] D. Jang, T. Gruner, A. Steppke, K. Mitsumoto, C. Geibel, and M. Brando, Large magnetocaloric effect and adiabatic demagnetization refrigeration with  $\text{YbPt}_2\text{Sn}$ , *Nat. Commun.* **6**, 8680 (2015).
- [51] Y. Tokiwa, B. Piening, H. S. Jeevan, S. L. Budko, P. C. Canfield, and P. Gegenwart, Super-heavy electron material as metallic refrigerator for adiabatic demagnetization cooling, *Sci. Adv.* **2**, e1600835 (2016).
- [52] P. Gegenwart, Grüneisen parameter studies on heavy fermion quantum criticality, *Rep. Prog. Phys.* **79**, 114502 (2016).
- [53] Y. Shimura, K. Watanabe, T. Taniguchi, K. Osato, R. Yamamoto, Y. Kusanose, K. Umeo, M. Fujita, T. Onimaru, and T. Takabatake, Magnetic refrigeration down to 0.2 K by heavy fermion metal  $\text{YbCu}_4\text{Ni}$ , *J. of Appl. Phys.* **131**, 013903 (2022).
- [54] A. Honecker and S. Wessel, Magnetocaloric effect in quantum spin-s chains, *Condens. Matter Phys.* **12**, 399 (2009).
- [55] B. Wolf, Y. Tsui, D. Jaiswal-Nagar, U. Tutsch, A. Honecker, K. Remović-Langer, G. Hofmann, A. Prokofiev, W. Assmus, G. Donath, and M. Lang, Magnetocaloric effect and magnetic cooling near a field-induced quantum-critical point, *Proc. Natl. Acad. Sci.* **108**, 6862 (2011).
- [56] M. Lang, B. Wolf, A. Honecker, Y. Tsui, D. Jaiswal-Nagar, U. Tutsch, G. Hofmann, A. Prokofiev, P. T. Cong, N. Krüger, F. Ritter, and W. Assmus, Magnetic cooling through quantum criticality, *J. Phys.: Conf. Series* **400**, 032043 (2012).
- [57] S. Bachus, D. A. S. Kaib, Y. Tokiwa, A. Jesche, V. Tsurkan, A. Loidl, S. M. Winter, A. A. Tsirlin, R. Valentí, and P. Gegenwart, Thermodynamic perspective on field-induced behavior of  $\alpha$   $\text{RuCl}_3$ , *Phys. Rev. Lett.* **125**, 097203 (2020).
- [58] J. V. José, L. P. Kadanoff, S. Kirkpatrick, and D. R. Nelson, Renormalization, vortices, and symmetry-breaking perturbation

- tions in the two-dimensional planar model, *Phys. Rev. B* **16**, 1217 (1977).
- [59] R. Moessner, S. L. Sondhi, and P. Chandra, Two-dimensional periodic frustrated ising models in a transverse field, *Phys. Rev. Lett.* **84**, 4457 (2000).
- [60] R. Moessner and S. L. Sondhi, Ising models of quantum frustration, *Phys. Rev. B* **63**, 224401 (2001).
- [61] S. V. Isakov and R. Moessner, Interplay of quantum and thermal fluctuations in a frustrated magnet, *Phys. Rev. B* **68**, 104409 (2003).
- [62] S. K. Baek, P. Minnhagen, and B. J. Kim, Kosterlitz-Thouless transition of magnetic dipoles on the two-dimensional plane, *Phys. Rev. B* **83**, 184409 (2011).
- [63] A. P. Gottlob and M. Hasenbusch, Critical behaviour of the 3D XY-model: a Monte Carlo study, *Physica A: Statistical Mechanics and its Applications* **201**, 593 (1993).
- [64] T. Numazawa, K. Kamiya, P. Shirron, M. DiPirro, and K. Matsumoto, Magnetocaloric effect of polycrystal GdLiF<sub>4</sub> for adiabatic magnetic refrigeration, *AIP Conference Proceedings* **850**, 1579 (2006).
- [65] P. Wikus, E. Canavan, S. T. Heine, K. Matsumoto, and T. Numazawa, Magnetocaloric materials and the optimization of cooling power density, *Cryogenics* **62**, 150 (2014).
- [66] A. Y. Vasiliev, A. E. Tarkhov, L. I. Menshikov, P. O. Fedichev, and U. R. Fischer, Universality of the Berezinskii–Kosterlitz–Thouless type of phase transition in the dipolar XY-model, *New J. Phys.* **16**, 053011 (2014).
- [67] S. Guo, A. Ghasemi, C. L. Broholm, and R. J. Cava, Magnetism on ideal triangular lattices in NaBaYb(BO<sub>2</sub>)<sub>2</sub>, *Phys. Rev. Mater.* **3**, 094404 (2019).
- [68] Y. Tokiwa, S. Bachus, K. Kavita, A. Jesche, A. A. Tsirlin, and P. Gegenwart, Frustrated magnet for adiabatic demagnetization cooling to milli-kelvin temperatures, *Commun. Mater.* **2**, 42 (2021).
- [69] A. Jesche, N. Winterhalter-Stocker, F. Hirschberger, A. Bellon, S. Bachus, Y. Tokiwa, A. A. Tsirlin, and P. Gegenwart, Adiabatic demagnetization cooling well below the magnetic ordering temperature in the triangular antiferromagnet KBaGd(BO<sub>3</sub>)<sub>2</sub>, [arXiv:2212.12483](https://arxiv.org/abs/2212.12483) (2022).
- [70] C. Hagmann and P. Richards, Two-stage magnetic refrigerator for astronomical applications with reservoir temperatures above 4 K, *Cryogenics* **34**, 221 (1994).
- [71] A. W. Sandvik, Computational studies of quantum spin systems, *AIP Conf. Proc.* **1297**, 135 (2010).
- [72] M. Creutz, Overrelaxation and monte carlo simulation, *Phys. Rev. D* **36**, 515 (1987).

# Supplementary Materials

## Dipolar Spin Liquid Ending with Quantum Critical Point in a Gd-based Triangular Magnet

Xiang *et al.*

### SAMPLE PREPARATION AND STRUCTURE CHARACTERIZATION

Polycrystalline samples of KBGB were firstly prepared by standard solid-state reaction method as reported in Ref. 40. Stoichiometric mixtures of  $\text{K}_2\text{CO}_3$  (99.99%),  $\text{BaCO}_3$  (99.95%),  $\text{H}_3\text{BO}_3$  (99.99%) and  $\text{Gd}_2\text{O}_3$  (99.99%) (with 6% excess  $\text{H}_3\text{BO}_3$  and 5% excess of  $\text{K}_2\text{CO}_3$  and  $\text{BaCO}_3$ ) were thoroughly ground and pelletized. Then the pellet was placed into an aluminum crucible and sintered at  $900^\circ\text{C}$  in air for 10 h. This sintering process was repeated for several times to minimize possible impurities.

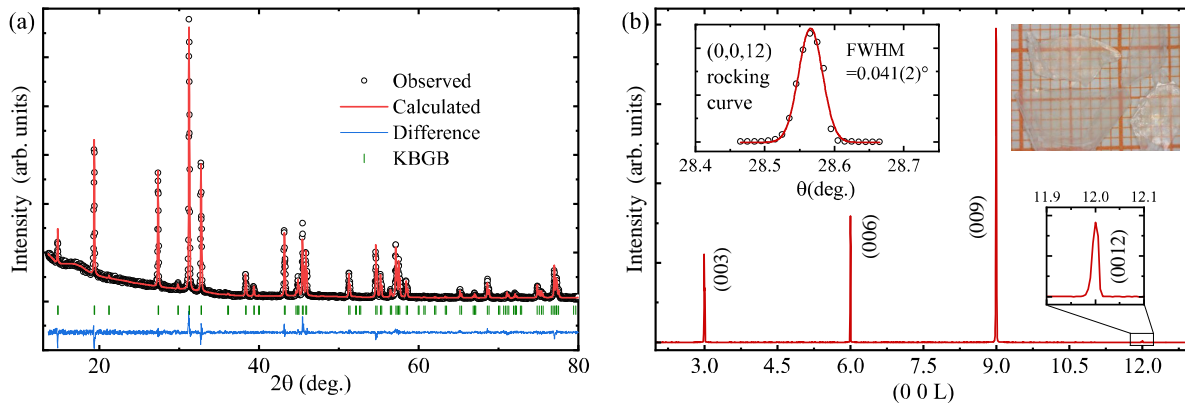


FIG. S1. (a) shows the powder XRD pattern of KBGB measured at room temperature and corresponding Rietveld refinement. The open circle and red solid line represent the observed and calculated intensities, respectively, while the blue solid line shows their difference. The olive vertical bars mark the expected reflections for KBGB. (b) Single-crystal XRD scan along the  $(0,0,L)$  direction for one representative crystal, revealing only peaks that are well indexed by  $(0,0,3n)$ . The insets show the image of the as-grown KBGB crystals and the rocking-curve scan of the  $(0,0,12)$  reflection fitted by a Gaussian profile. The very narrow peak width of  $\text{FWHM} = 0.041^\circ$  indicates excellent quality of the crystals.

Single-crystal samples of KBGB were grown using the flux method as reported in Ref. 41. The pre-obtained polycrystalline KBGB with high purity was mixed with the  $\text{H}_3\text{BO}_3$  (99.99%) and  $\text{KF}$  (99.9%) fluxes in a molar ratio of 2:3:[2-3], and thoroughly ground. The mixture was transferred into a Pt crucible, heated up to  $980^\circ\text{C}$  in air for 24 h, and then slowly cooled to  $790^\circ\text{C}$  with a rate of  $2^\circ\text{C}/\text{h}$ . After the furnace cooling, centimeter-sized crystals were obtained on top of the fluxes.

The phase purity of the polycrystalline KBGB sample was confirmed by powder XRD at room temperature, performed on a Bruker D8 ADVANCE diffractometer in Bragg-Brentano geometry with  $\text{Cu-K}\alpha$  radiation ( $\lambda = 1.5406 \text{ \AA}$ ). As shown in Fig. S1(a), the powder XRD pattern can be well fitted with the previously reported trigonal phase of KBGB [40] ( $a = b = 5.4676(1) \text{ \AA}$ ,  $c = 17.9514(3) \text{ \AA}$ ), without any visible impurity peaks, indicating high purity of the synthesized KBGB powders. The quality of the single-crystal KBGB sample was checked by high-resolution synchrotron XRD ( $\lambda = 1.54564 \text{ \AA}$ ) measurements at room temperature, performed on the 1W1A beamline at the Beijing Synchrotron Radiation Facility (BSRF), China. As shown in Fig. S1(b), a long  $L$  scan, equivalent to a  $\theta$ - $2\theta$  scan with respect to the normal direction of the plate-like KBGB crystal, only shows Bragg reflections well indexed by  $(0, 0, 3n)$  as expected for the  $R\bar{3}m$  space group. The peak width (full width at half maximum, FWHM) observed in the rocking-curve scan of the  $(0, 0, 12)$  peak is very small,  $0.041(2)^\circ$ , as shown in the inset of Fig. S1(b), which suggests excellent crystal quality. KBGB is relatively easy to synthesize and has excellent chemical stability, paving its viable way for applications in advanced cryogenics.



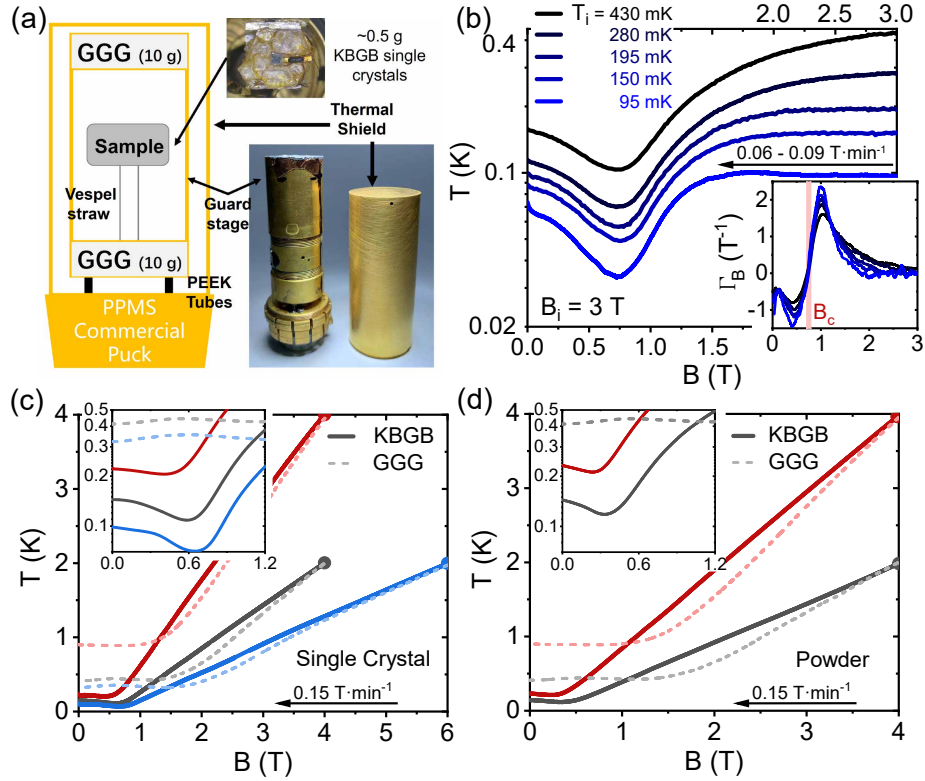


FIG. S2. (a) Illustration and photo of the quasi-adiabatic two-stage demagnetization cooling device, KBGB single crystals used in the measurements are also shown. (b) shows the DR-based measurements on 2.3 mg single crystal from an initial temperature  $T_i \leq 430$  mK and field  $B_i = 3$  T, where the lowest achieved temperature is  $T_m \simeq 33$  mK. The inset shows the magnetic Grüneisen ratio  $\Gamma_B$  deduced from the low-temperature isentropic  $T$ - $B$  lines in the main plot, where the sign change is evident and the peak becomes more and more pronounced as the initial temperature  $T_i$  lowers. (c) presents the PPMS-based measurements of isentropic curves on 0.5 g KBGB single crystals starting from various initial conditions ( $T_i = 2$  K,  $B_i = 4$  T), (2 K, 6 T), and (4 K, 4 T), respectively, where the lowest temperatures are found to be significantly lower than those of GGG with the same initial conditions. The inset zooms in the low-field ( $B \leq 1.2$  T) and low-temperature ( $T_i \leq 500$  K) regime. (d) Demagnetization cooling measurements of 3 g pellet consisting of powder samples (1.5 g KBGB and 1.5 g Ag), where the obtained lowest temperature are slightly higher compared to single-crystal KBGB sample measurements, yet much lower than that of GGG [same data as in (b) panel] under the same condition. The field sweep rates in the demagnetization process are 0.15 T/min for PPMS-based measurements ( $T_i \geq 2$  K) and 0.06-0.09 T/min for DR-based measurements ( $T_i \leq 430$  mK).

### THERMODYNAMIC AND MAGNETOCALORIC MEASUREMENTS

Comprehensive magnetothermal measurements were performed on single-crystal samples of KBGB. The low-temperature specific heat ( $C_p$ ) and ac susceptibility ( $\chi_{ac}$ ) measurements were conducted using the Quantum Design Physical Property Measurement System (PPMS) equipped with a <sup>3</sup>He-<sup>4</sup>He dilution refrigerator (DR) insert. The specific heat data were measured under various out-of-plane fields ( $B//c$ ) with the semi-adiabatic heat pulse method. The phonon contributions are negligible ( $C_{ph}/T \lesssim 0.003$  J mol<sup>-1</sup> K<sup>-2</sup> below 2 K) based on Debye  $T^3$  analysis of high-temperature  $C_p$  data. The ac susceptibility  $\chi_{ac}$ , as a function of temperature, was measured in zero dc field under different ac frequencies, with the amplitude of the ac excitation field set as 3 Oe. The dc magnetic susceptibility  $\chi_{dc}$ , as a function of temperature down to 0.4 K, was measured using a Quantum Design Magnetic Property Measurement System (MPMS) equipped with a <sup>3</sup>He insert. The isothermal dc magnetization curves in the field up to 7 T applied along the  $a$  and  $c$  axes were measured at 0.4 K with the same setup.

Magnetocaloric effect (MCE) of the frustrated dipolar magnet KBGB was characterized using a homemade setup integrated into the PPMS, for initial temperature  $2$  K  $\leq T_i \leq 4$  K. A DR-based setup is also exploited for MCE measurements with low

initial temperature  $T_i \leq 500$  mK.

### PPMS-based setup for quasi-adiabatic demagnetization measurements

Figure S2(a) shows a homemade, PPMS-based construction for quasi-adiabatic demagnetization process, which is inspired by the Hagmann-Richards design of two-stage adiabatic demagnetization refrigeration for space applications [70]. An additional guard stage with  $\text{Gd}_3\text{Ga}_5\text{O}_{12}$  (GGG) single crystals (20 g) serve as the thermal intercept between the KBGB sample stage and the PPMS chamber. In experiments, plate-like KBGB single crystals (with a total mass of 0.5 g) are stacked along the  $c$ -axis and fixed on a silver foil by cryogenic glue. We also perform demagnetization measurements on pellet with KBGB and Ag powders 1:1 in mass, where Ag powders are introduced to enhance the thermal conductivity. A Vespel straw is used to support the sample pillar inside the copper cylinder, which improves its thermal insulation to the PPMS chamber. The guard stage is supported by PEEK tubes to reduce the thermal exchange with chamber environment. The electrical connection of the thermometer (a field-calibrated  $\text{RuO}_2$  chip) on top of the pillar is made by two pairs of twisted manganese wires (25  $\mu\text{m}$  in diameter and approximately 60 cm in length) to reduce the heat leak. A thermal shield protects the sample from radiant heating as well as other parasitic heat loads from the chamber. Demagnetization cooling measurements are performed by gradually decreasing the fields from the initial field  $B_i$  at a rate of  $\dot{B} = 0.15 \text{ T}\cdot\text{min}^{-1}$ .

The total parasitic heat load in the PPMS chamber can be estimated from the temperature changing rate of sample after the magnet field is exhausted, *i.e.*, in the hold process with  $B = 0$ . To be specific, the heat load is estimated by  $\dot{Q} = C_0 \dot{T}$ , where  $C_0$  is heat capacity of the sample and  $\dot{T}$  is the temperature change rate. For example, when starting from an initial condition of 2 K, it is found that  $\dot{T} \approx 5 \times 10^{-6} \text{ K/s}$ . Considering  $C_0 \approx 0.01 \text{ J/K}$  for 0.5 g KBGB samples in the relevant temperature range, we thus figure out that the parasitic heat load is  $\dot{Q} \approx 0.05 \mu\text{W}$  for 2 K environment.

In Figs. S2(c,d) we show the isentropic lines of KBGB obtained through the quasi-adiabatic demagnetization measurements, and make a comparison with the widely used refrigerant GGG. The results with different initial conditions lead to the same conclusion, given it single-crystal or powder samples, that KBGB clearly outperforms GGG in the reached lowest cooling temperature. For example, from  $T_i = 2 \text{ K}$  and  $B_i = 4 \text{ T}$ , single-crystal KBGB sample (0.5 g) can reach as low as  $T_m \simeq 108 \text{ mK}$ , and powder sample (1.5 + 1.5 g) to  $T_m \simeq 118 \text{ mK}$ , both of which are much lower than  $T_m \simeq 412 \text{ mK}$  of GGG (20 g).

### The DR-based quasi-adiabatic demagnetization measurements

To perform MCE measurements from a lower initial temperature below 500 mK, a standard DR heat capacity sample mount is used, which provides a quasi-adiabatic condition with high vacuum in the  $^3\text{He}$ - $^4\text{He}$  dilution insert of PPMS. The thermometer used is also  $\text{RuO}_2$  semiconductor, which has been carefully calibrated under various magnetic fields (0-5 T) and till very low temperature (50 mK-4 K), further extrapolated to 30 mK according to the scaling behavior  $\ln(R - R_0) \sim T^{-1/4}$  [68].

The polymer strips are used to support the sample platform. A KBGB single crystal with much smaller mass of 2.3 mg is used here, to avoid large magnetic torque that may break the suspended lines in the sample mount. To decrease the irreversible heating effect on the DR mount, the field sweep rate  $\dot{B}$  has been reduced to 0.06 - 0.09  $\text{T}\cdot\text{min}^{-1}$ . Due to the small mass of the sample, the parasitic heat loads have a stronger influence in the DR-based MCE measurements (than that in the PPMS-based measurements). In Fig. S2(b), a prominent dip can be observed in the isentropic lines, which leads to the diverging peaks and dips with a sign change in the inset, again indicating clearly the existence of a QCP.

### MONTE CARLO SIMULATIONS

As the spin quantum number  $S = 7/2$  is relative large, we use the classical Monte Carlo simulations with standard Metropolis algorithm and single spin update to study the DH model for KBGB [71, 72]. The largest system size involved in the simulations

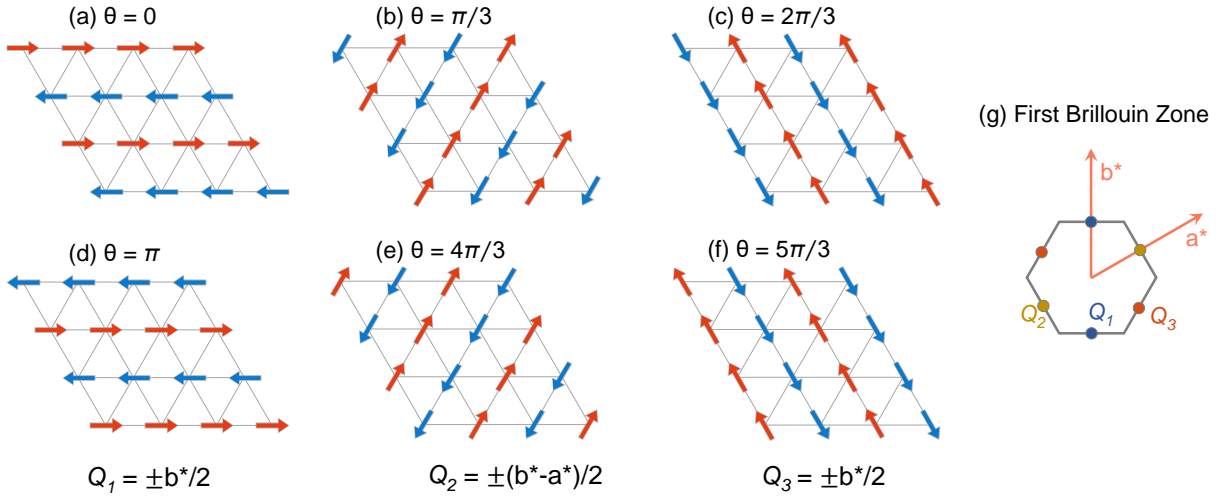


FIG. S3. (a)-(f) show the magnetic configurations of the stripe order with 6-fold degeneracy, *i.e.*, 6-clock AF, which can be labeled with angle  $\theta$  (in complex order parameter  $\Psi_{xy}$ ), and also by ordering vector  $Q_1$  (blue dots),  $Q_2$  (yellow dots), and  $Q_3$  (red dots) shown in (g).

is  $60 \times 60$ . We show the 6-fold degenerate ground-state spin configurations in Figs. S3(a-f), where the corresponding ordering wave vectors  $Q = \pm \frac{1}{2}a^*, \pm \frac{1}{2}b^*, \pm \frac{1}{2}(a^* - b^*)$  with  $a^*, b^*$  the primary vectors in the reciprocal lattice [see Fig. S3(g)].

In Fig.1(c-e) of the main text, we show histograms of the complex order parameter  $\Psi_{xy} \equiv me^{i\theta}$  under magnetic field  $B = 0.68$  T and at different temperatures, *i.e.*, (c)  $T = 0.05$  K (6-clock AF), (d)  $T = 0.14$  K (DSL), and (e)  $T = 0.25$  K (PM), respectively. To count the histograms, we collect  $5 \times 10^6$  MC samples on a  $L = 12 \times 12$  lattice for statistics. Note the phase angle  $\theta$  of the complex  $\Psi_{xy}$  can only take 6 discretized values, and the effective theory is a 6-clock model with the order parameter  $\Psi_{xy}$ .

The MC simulation results of specific heat are shown in Fig. S4, where the contour plot in Fig. S4(a) resembles the experimental data in Fig. 3(b) of the main text. The peak in  $C_m$  is located at about 270 mK, and the peak heights are converged with system sizes, as indicated in the inset of Fig. S4(b). In Fig. S4(c), we apply out-of-plane fields and observe that the  $C_m$  peaks move towards low-temperature side with heights lowered, in agreement with the experimental measurements shown in Figs. 2(a,b) of the main text.

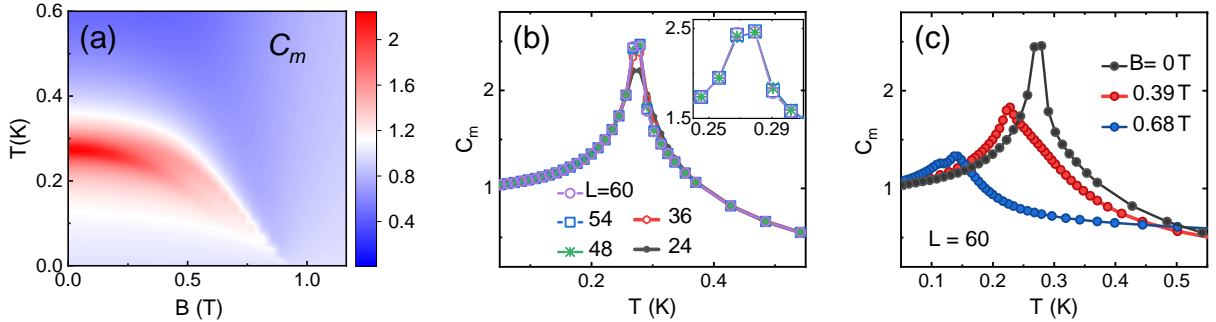


FIG. S4. The calculated results of specific heat  $C_m$ . (a) shows the contour plot of  $C_m$  data under out-of-plane fields. The  $C_m$  curves (b) under zero-field for different system sizes and (c) with a fixed size  $L = 60$  and under various fields are presented. The inset in (b) zooms in the  $C_m$  data near the crossover temperature of about 270 mK. The MC simulations are performed on the HD model [Eq. (1) in the main text] with couplings  $J = 47$  mK and  $D = 80$  mK.

In the MC calculations, we use the natural unit ( $J = 1$ ) and the following process is required for comparing the model simulations to experiments: (1) We replace the  $S_i$  operators in Eq. (1) of the main text by classical vectors, *i.e.*,  $S_i \rightarrow S\mathbf{n}_i \equiv$

$7/2 \mathbf{n}_i$ , where  $\mathbf{n}_i$  is a unit vector; (2) The value of temperature  $T$  in natural unit is multiplied by a factor of  $J = 0.047$  K; (3) Multiply the magnetic field  $B$  in natural unit (*i.e.*,  $B/JS = 1$ ) by a factor of  $Jk_B/(g_c\mu_B) \simeq 0.028$  T.